PbS and InAs Quantum-Dot Thin Films for Short-Wave Infrared Detectors

Abu Bakar Siddik[1,2], Epimitheas Georgitzikis[1]*, Wenya Song[1], Athina Papadopoulou[1,2], Arman Uz Zaman[1], Myung Jin Lim[1], Vladimir Pejovic[1], Itai Lieberman[1], Pawel E. Malinowski[1], Jan Genoe[1,2], Thierry Conard[1], David Cheyns[1] and Paul Heremans[1,2].*

[1]IMEC, Kapeldreef 75, 3001 Leuven, Belgium.

[2]Dept. of Electrical Engineering ESAT, KU Leuven, Kasteelpark Arenberg 10, 3001 Leuven, Belgium.

ABSTRACT

Colloidal quantum dots (CQD) are cutting-edge optoelectronic semiconductor nanocrystals that enable short-wave infrared (SWIR) vision by widely tunable SWIR light absorption. Thanks to the advances in CQD surface ligands engineering, SWIR detectors, and emitters will soon find their way into products. The CQD-based optoelectronic devices are being optimized by adapting the size of CQDs and selection of the ligands and yet, the measurement schemes of energy band structure based on different ligands and processes of ligand exchange are not systematically studied. In this work, we systematically characterize the energy band structure of PbS (absorbing at different SWIR wavelengths) and InAs with various ligands, for both solid state and liquid phase ligand exchange processes (SSLE and LPLE), by using ultraviolet photoelectron spectroscopy

(UPS). The deduced energy band structures reveal that the apparent energy difference between the Fermi and valence band maximum, $|E_F-E_{VBM}|$, largely depends on the physical density and distribution of the CQDs within the probing area. Transmission electron microscopy (TEM) images, X-ray photoelectron spectroscopy (XPS), atomic force microscopy (AFM), and variable angle spectroscopic ellipsometry reveal details of CQD distribution, surface elemental profile, and topologies and how they affect the observed energy band structure. We demonstrate that the multi-step coating improves the CQD distribution and packing density resulting in more reliable and reproducible results that represent the bulk CQD film energy band structure. The comparison of solid and liquid phase ligand exchanged PbS and InAs SWIR CDQs energetics indicates that the LPLE ensures more uniform dispersion and high packing density of CQDs regardless of the solution concentration. The photoemission-deduced energy band structures are validated by fabricating thin film photodiodes using SWIR SSLE PbS and LPLE In(As,P) CQDs. The Fermi-referenced band structures of the fabricated full photodiode stacks including band offsets and bending are discussed to improve our understanding of the device working principles and to optimize the devices further.

KEYWORDS

Colloidal quantum dot, PbS, InAs, solid-state ligand exchange, liquid-phase ligand exchange, photoelectron spectroscopy, transmission electron microscopy, energy band structure

1. INTRODUCTION

The pursuit of short-wave infrared (SWIR) light absorbers is increasingly captivating, owing to their vast potential in various optoelectronic applications such as photodetectors, solar cells,

phototransistors, and light-emitting diodes (LEDs) [1–6]. In the last decades, a new class of material namely colloidal quantum dots (CQDs) has emerged, that exhibits sensitivity throughout the entire SWIR spectrum, a spectral domain interesting for a wide range of consumer electronic technologies including photo-harvesting, imaging, sensing, and communication [7–10]. Thanks to the extensive effort towards the synthesis of the CQDs, these materials now comprise a wide variety of semiconductors such as PbS, InAs, InP, PbSe, HgTe, and InSb [11–18]. Synthesis-dependent optoelectronic properties, quantum confinement, large-area solution processability, and band gap tunability make them attractive choices for thin-film SWIR detectors [1,7,19–21]. These thin-film detectors can be monolithically integrated on silicon read-out circuits (ROIC) to develop high-resolution thin-film SWIR imager which is an attractive cost-effective alternative to traditional flip-chip bonded III-V based SWIR imagers [7,13,14,22].

The surface passivation of CDQs, better known as ligands, plays a crucial role in determining the electronic properties [14,23–26]. Depending on the type of ligands and method of ligand exchange, the energy band structure, doping profile and concentration, trap distribution, and density can be tuned for the specific device of interest [2,12,20,24,25,27,28]. It is immensely important to understand the energy band structures based on various ligand types, synthesis methods, and sizes of these quantum-confined nanocrystals to engineer thin-film electronic devices. However, the lack of systematic studies and inconsistency among the reported energy band structures in the literature hinders the effort toward efficient device design and simulation [24,25,27,28]. More specifically the study of the energy band structure of both solid-state ligand exchange (SSLE) and liquid-phase ligand exchange (LPLE) for both mainstream PbS and InAs CQDs has not been reported. In SSLE, the native ligands (e.g. oleic acid) of the parent CQDs are typically exchanged step by step on the CDQ solid film by dispersing the solution of the ligands on the film for a certain time, followed

by washing steps to remove the excess ligands [4,5,7,29]. Such step-by-step coating of CDQ and subsequent ligand exchange together with the washing steps, may affect the dispersion of CQDs and their electronic band structure [5,29–31]. On the other hand, in LPLE, the ligands are exchanged already in the liquid phase, which is desirable for industry as it allows one-step coating in a mass production environment [32,33]. Thus, the study of electronic band structures comprising both SSLE and LPLE is essential.

X-ray and ultraviolet photoelectron spectroscopy (XPS and UPS) are considered the gold standard to analyze the occupied density of states (DOS) [27,34]. Because of the higher ionization cross-section of valence electrons, UPS is widely utilized to determine the valence band DOS [34]. The difference between the Fermi edge and valence band minimum (VBM) of UPS spectra provides crucial information about the type of semiconductor and doping concentration. However, one should be careful when analyzing the CQD thin-film UPS spectra, as the measurement can be affected by the type of ligands utilized, the exchange process, dispersion on the substrate, and the thickness of the film. Miller et al. reported that the $|E_F\text{-}E_{VBM}|$ can be overestimated due to low DOS at the valence band edge resulting in $|E_F\text{-}E_{VBM}|>E_g$ and easily misinterpreted as a degenerate semiconductor based on their finding of the lack of DOS at the Fermi edge [27]. Zhang et al. characterized such energy band structure as degenerate/high doping based on the intraband transition observed in heavily doped SWIR PbS CQD thin films by Ramiro et al. [35,36]. In this article, we demonstrate a similar effect of such overestimated $|E_F\text{-}E_{VBM}|$ due to lack of physical packing density and dispersion of the PbS and InAs CQDs in the thin films, especially for SSLE. Our study showcases that a carefully designed UPS measurement protocol coupled with proper thin film preparation can improve the precision and reproducibility of measured energy band

structures of the CDQ films, which will in turn advance our understanding and optimization of thin film devices.

We characterize the energy band structure of PbS and InAs SWIR CDQ thin films of various nanoparticle sizes, ligands and two ligand exchange processes. For both PbS and InAs thin films, we show that by improving the physical packing density and dispersion of the CQDs, the DOS signal at the valence band edge can be amplified when measuring UPS spectra. Ellipsometry measurements show that a single-step-coated SSLE PbS and InAs offer thickness over 30 nm which is greater than the UPS information depth ($\leq$5 nm) [34]. Because of the poor distribution and packing density of CQDs, the valence band DOS near the Fermi edge is not detectable, thus, the deduced band structure becomes $|E_F-E_{VBM}|>E_g$. However, in the presence of degenerate/high doping, the expected populated DOS may not be detected by photoemission due to intrinsic low conduction band edge of CQDs [37]. Transmission electron microscopy (TEM), XPS narrow band spectra, ellipsometry, and atomic force microscopy data confirm that increasing the number of steps of deposition in SSLE boosts VBM signal by improving the CQD dispersion and packing density. Image processing of TEM images further affirms that the CQD coverage of 53.28% for 1-step coating increases to 90.62% in 2-step coating within a TEM imaging area of 275*275 nm^2. On the other hand, the LPLE PbS and In(As,P) CDQ films show no variation in E_F-E_{VBM} for different concentrations of solution, making LPLE process a better choice for UPS analysis. Fabricated thin film P-N junction PbS and In(As,P) quantum dot photodiodes (QDPD) validate the results of the UPS spectra, and the deduced Fermi reference band diagram gives valuable insight into thin film QDPD optimization.

2. RESULTS AND DISCUSSION

2.1 Solid-sate ligand exchange (SSLE)

Solid state ligand exchange of CQDs is widely utilized to exchange ligands from the original long, electrically isolating ones to conductive and surface passivating ones. First, a solid CQD thin film is fabricated on a substrate by solution process coating (spin, spray, dip, or drop coating), and then a separate solution containing the target ligands is applied for a certain time to let the native ligand exchange [4,5,7,29]. It is also common to use additional washing steps with the solvent to wash away the residues [4,5,7,29]. The process needs to be repeated many times to achieve the desired thickness for a certain device. Naturally in this process, the concentration of the parent CDQ solution is kept low to make sure of successful ligand exchange after each step. Unless otherwise stated for SSLE we prepare thin films from a 40 mg/mL (~30 nm thick film for a single step) oleic acid-capped PbS parent solution in octane as optimized for our previously reported thin film photodetector and

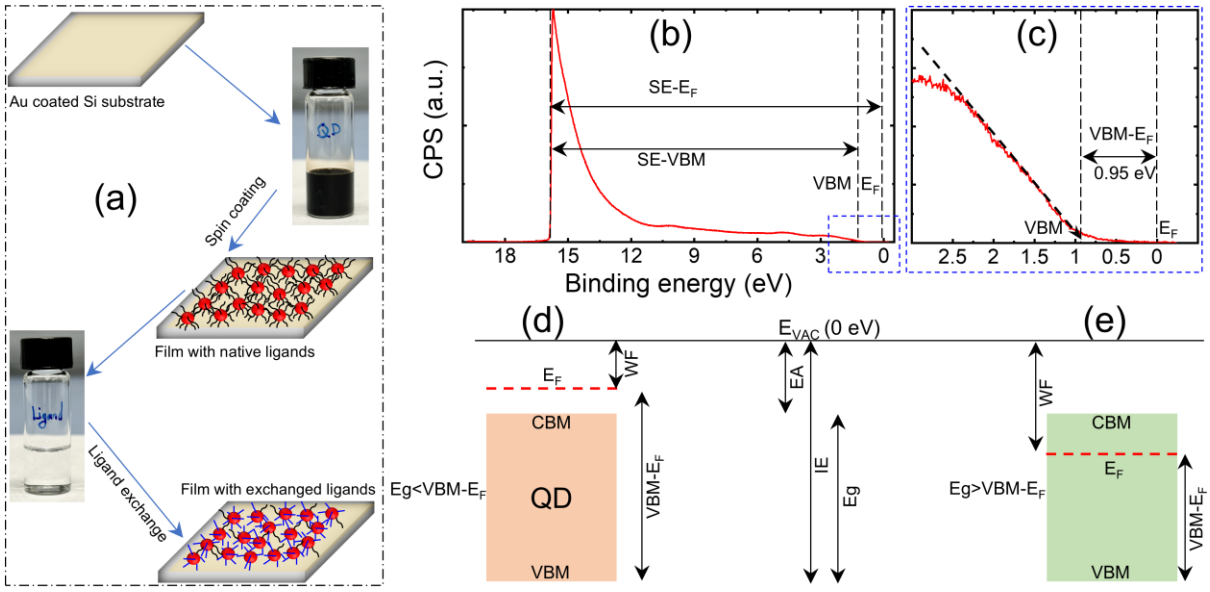


Figure 1. (a) Schematic of thin film preparation from the CQD with long electrically isolating native ligands and SSLE process with shorter conductive and surface passivating ligands. (b) Full UPS spectra of SSLE 1-step coated 1520 nm (E_g= 0.82 eV) PbS ZnI_2 MPA showing secondary electron (SE) cutoff, valence, and Fermi edges; (c) detailed valence band edge. (d) The energy band diagram deduced from (b)-(c) seems to show $|E_F\text{-}E_{VBM}|>E_g$; (e) the expected energy band diagram would feature $|E_F\text{-}E_{VBM}|<E_g$.

imager applications [7,13]. We study the most widely utilized Zn-halides (I_2, Br_2, Cl_2) with a mixture of 3-mercaptopropionic acid (MPA) and 1,4 benzenedithiol (BDT) as ligands for SSLE of PbS CQDs with excitonic peaks at 1520 nm, 1420 nm, 1280 nm, and 940 nm. The optical bandgaps and physical sizes of the nanocrystals of all CQDs of various sizes utilized in this study are tabulated in Table S1.

UPS spectra of a single step coated SSLE PbS ZnI_2 MPA with the excitonic peak at 1520 nm in Figure 1a-b seem to indicate that $|E_F-E_{VBM}|>E_g$. The corresponding energy band diagram in Figure 1c is, however, only valid for a metal or a degenerate semiconductor, while the lack of DOS at E_F (0 eV binding energy) suggests otherwise, as Miller et al. also reported [27]. On the other hand, a $|E_F-E_{VBM}|<E_g$ case would deduce an energy band structure as depicted in Figure 1d. The ellipsometry results in Figure S1a indicate that single-step coating produces ~34 nm thick film which should be suitable for UPS measurement, as it is significantly higher compared to the UPS information depth [34]. At this point, we hypothesize that the dispersion of CQDs can play a significant role in explaining the anomaly that $|E_F-E_{VBM}|$ appears to be larger than E_g, as the UPS beam size is relatively large ~1 mm^2. Aiming to improve the CQD dispersion so that we can include more dots within the probing area, we increased the number of deposition steps to 2, 3,

and 5, resulting in 61, 89, and 138 nm thick films, as shown respectively in Figure S1a. The results are also in line with the thicknesses measured by the profilometer in our recent report [38].

Figure 2 shows the UPS spectra of the valence band edge of PbS CQD with varying excitonic peaks at 1520, 1420, 1280, and 940 nm. These spectra correspond to SSLE PbS CQD thin films with ZnI_2 MPA (Figure 2a-d) and BDT (Figure 2e-h) ligands and are prepared by 1, 2, 3, and 5-step coating processes. The full UPS spectra of the corresponding valence band edges and the extracted differences between valence band maximum (VBM) and Fermi edge $|E_F\text{-}E_{VBM}|$ are included in Figure S2 and Table S2, respectively. Here, Figure 2a (1520 nm PbS ZnI_2 MPA) shows a significant increase in VBM DOS signal along with a more pronounced shape as the number of deposition steps increases. Note that the VBM edge values fall on the same point when taking the linear regressions for 2, 3, and 5-step deposited films. As can be seen from Figure 2a inset, the $|E_F\text{-}$

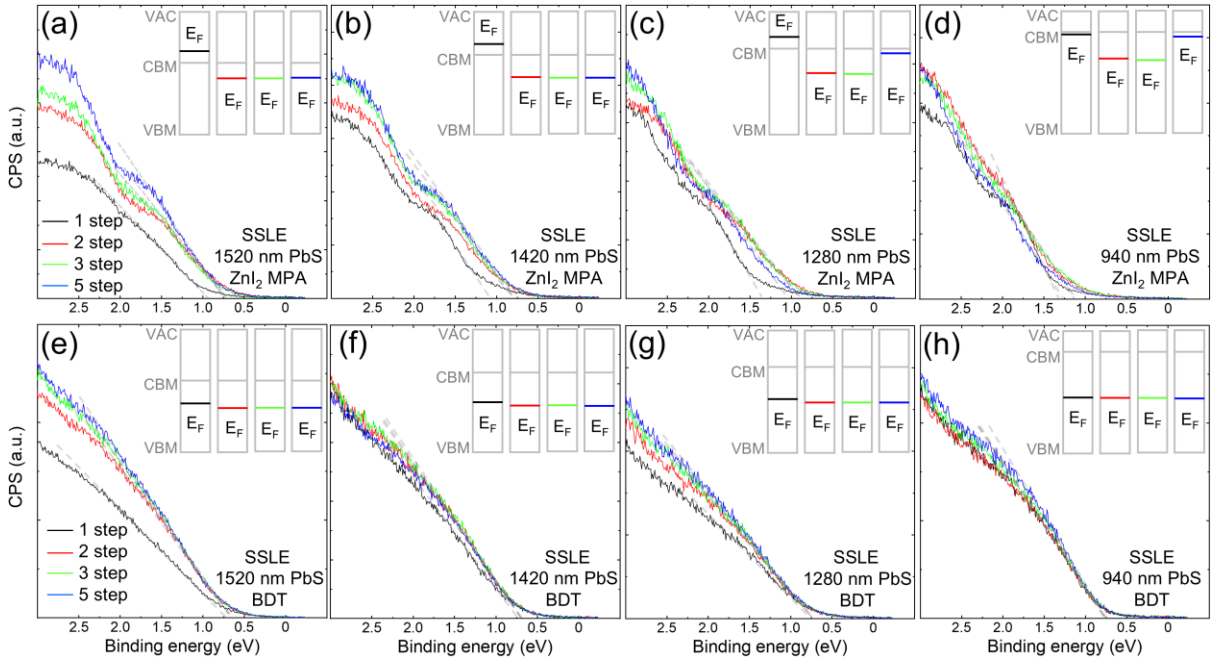


Figure 2. (a)-(d) UPS spectra showing valence band edge of 1, 2, 3 and 5 step deposited SSLE PbS ZnI_2 MPA thin-films for PbS CQD absorbing at 1520, 1420, 1280 and 940 nm, respectively. UPS spectra for SSLE PbS films with BDT ligand in (e)-(h). All the insets denote $|E_F\text{-}E_{VBM}|$ of respective spectra. The complete UPS spectra with secondary electron (SE) emission edge of all these valence band edge profiles are plotted in Figure S2.

$E_{VBM}|$ becomes smaller than E_g and stays consistent for 2, 3, and 5-step depositions. Therefore, the surface topologies, chemical species, and distribution of CQDs are expected to be alike for 2 deposition steps or more. As the absorption peaks move towards shorter wavelengths from 1520 nm to 1420 nm, 1280 nm, and 940 nm, we observe the consistent behavior of $|E_F-E_{VBM}|>E_g$ in Figure 2b-d for single step-coated SSLE PbS ZnI_2 MPA which does not represent the energy band structure of bulk thin films. Although is clear from the UPS spectra that the number of steps in SSLE deposition essentially improves the VBM signal, one should be careful during data acquisition, especially for thicker layers because of potential charging effects. For the dots with excitonic peaks at 1280 nm and 940 nm, we observe charging effects for thick layers (5-step deposition), by live shift of data towards higher binding energy during data acquisition, which can lead to erroneous results as can be seen in Figure 2c-d and insets. Therefore, it is important to optimize the number of SSLE deposition steps for any new type of quantum dots, ligands, the substrates to achieve this trade-off between the best possible DOS signal and charging effect. Figure 2e-f shows the UPS valence band edge spectra of the same quantum dots and the number of deposition steps for solid-state exchanged BDT ligand where we also observe a more consistent and overlapping $|E_F-E_{VBM}|$ for 2, 3, and 5-step depositions compared to 1-step deposition.

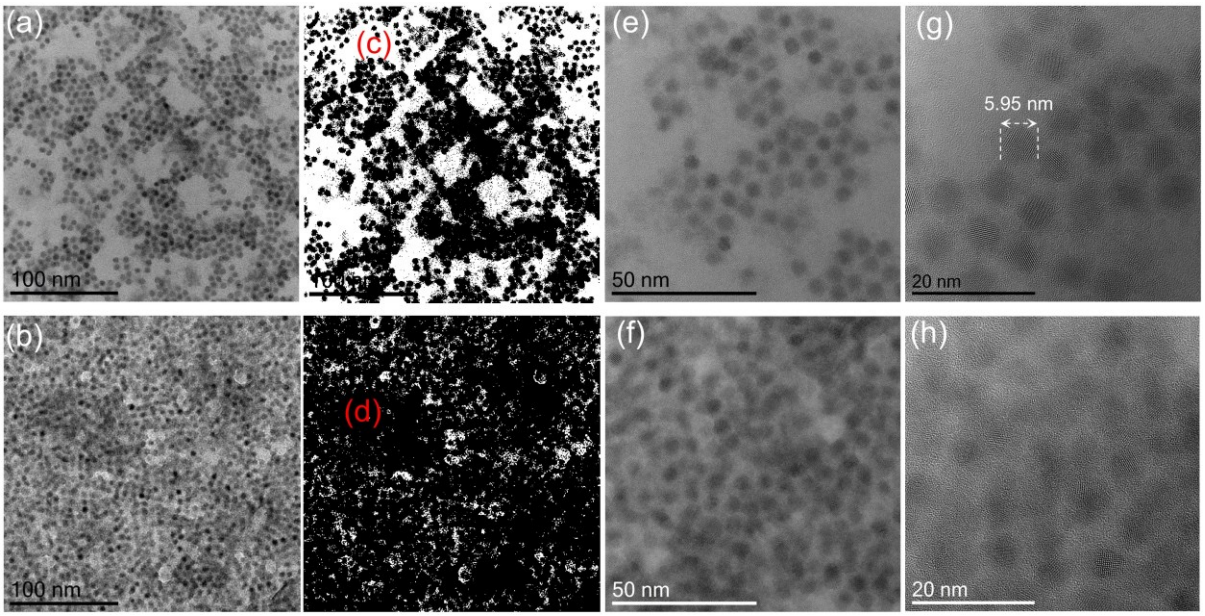


Figure 3. BF-TEM images of 1 and 2-step deposited SSLE PbS (1520 nm) ZnI_2 MPA films in (a)-(b), and their respective processed binary images in (c)-(d). The HR-TEM images of 1 and 2-step coated films are in (e)-(f), and (g)-(h), respectively.

To achieve a comprehensive overview of film quality and how it affects the UPS measurements, we systematically looked at various analysis and imaging techniques such as TEM, XPS, AFM, and ellipsometry. To begin with, the ellipsometry-deduced extinction coefficient (k) and refractive index (n), of deposited PbS (1520 nm) ZnI_2 MPA exhibit an increasing trend with the number of deposition steps (Figure S1b-c), which indicates an increasing film density [39,40]. A redshift of the absorption peak is also observed with increasing number of coating steps due to an enhanced electronic coupling resulting from the closely packed quantum dots [41,42]. We record XPS narrow band spectra (Figure S3) to evaluate the evolution of chemical species as we increase the number of SSLE deposition steps. The absence of Au peaks and lack of binding energy shifts despite the thickness variations suggest no sample-substrate interactions. A large increase in peak signal intensity by 35% and 32% is observed for Pb4f and S2s XPS narrow band spectra when moving from 1 to 2-step deposited film. On the other hand, the C1s, O1s, Zn2p3/2, and I3d5/2 originated

from exchanged ligands and residues drop by 50%, 22%, 46%, 5%, respectively. These findings clearly suggest a better dispersion and density of CQDs in the film in 2-step deposited compared to single-step SSLE coating. In addition, using C1s (284.8 eV) as the binding energy reference, the core-level spectra (Figure S3) are calibrated, and the $|E_F\text{-}E_{VBM}|$ values are extracted from the XPS VBM spectra (Table S3) which are in line with UPS data calibrated by the Fermi edge.

The transmission electron microscopy (TEM) images of 1 and 2-step coated PbS ZnI_2 MPA (1520 nm) films reveal a significant difference in CQD dispersion and density as demonstrated in Figure 3a-b. Using image processing binary imaging techniques, we separated the CQD coverage areas from the residues (anything other than CQDs) which shows (Figure 3c-d) that the CQD coverage area increases from 53.28% (1-step coating) to 90.62% (2-step coating). Further increasing the number of deposition steps can further increase CQD coverage, as suggested by both UPS and XPS spectra. High-resolution TEM (HR-TEM) images in Figure 3e,g and f,h further illustrate CQD dispersion, crystallinity, and the size of a single CQD particle for 1 and 2-step coatings, respectively. As explained earlier the XPS peak intensity of C1s, O1s, Zn2p3/2, and I3d5/2 decreases while the signal of Pb4f and S2s increases with the number of deposition steps, which also aligns with the elemental mapping (EDS) using the characteristic X-rays generated by an

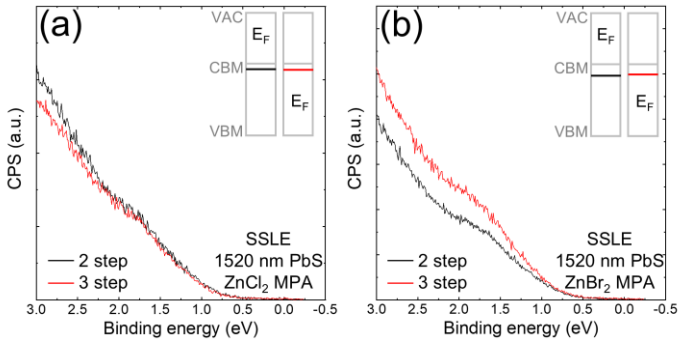


Figure 4. Valence band spectra and relative changes in $|E_F\text{-}E_{VBM}|$ of PbS $ZnCl_2$ MPA (a) and $ZnBr_2$ MPA (b) for 2, 3 step SSLE deposited thin CQD films.

electron-beam in Figure S4. In contrast, the atomic force microscopy (AFM) images (Figure S5) reveal RMS roughness of 2.86 nm, 2.49 nm, and 2.32 nm for 2, 3, and 5-step depositions in contrast to a high value of 4.77 nm for single-step coated film.

Metal halides are some of the most widely utilized ligands in the literature for PbS CQDs because of the anionic nature of most halide ions (e.g. I and Br) leading to preferential binding to lead-rich 111 facets of the PbS CQDs capped with the native oleate ligands [43]. Using single I, Br, Cl, or F halide ion ligands, the Fermi and ionization energies of PbS CDQs are reported to be tuned electronically to improve thin-film electronic device characteristics and stability [19,24,43,44]. Recent reports show that mixing these ions in different ratios and conditions can be very attractive to tune the electronic characteristics of PbS CQDs [24,44]. The literature interest in halide ions in PbS surface passivation motivated us to include the UPS measurements of SSLE PbS (1520 nm) CQDs of Br and Cl along with I (as showed earlier). As we found earlier for PbS ZnI_2 MPA, the optimum number of SSLE depositions to be 2 or 3 for UPS measurement, we directly fabricated films as such for PbS $ZnBr_2$ MPA and PbS $ZnCl_2$ MPA and VBM edges of these spectra are depicted in Figure 4a-b, respectively. Both the shape of the VBM and extracted $|E_F\text{-}E_{VBM}|$ (inset of Figure 4a-b) values validate that the optimized number of deposition steps 2, 3 can help to improve a more

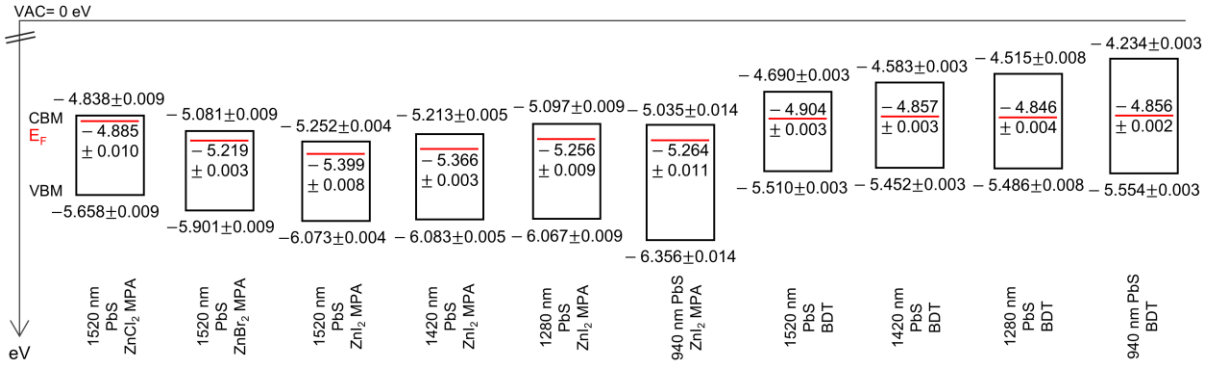


Figure 5. Summary of energy band structure PbS CQDs of various size and ligands (SSLE). The error bars calculated from the five data points represent the precision and reproducibility.

reliable energetic extraction of PbS CQDs. Figure 5 summarizes the energy band structures of PbS CQDs of different dot sizes and ligands (halides I, Br, Cl, and short thiol BDT). Keeping the size of the CQD identical while changing the halide ligand ions from Cl to I results in deepening ionization energy [25,28]. For a fixed halide ion ligand, I, increasing the bandgap (long to short wavelength absorption) results in increasing n-type behavior as $|E_F-E_C|$ (energy difference between Fermi and conduction band minimum) becomes smaller with respect to the bandgap. A completely opposite behavior is observed for BDT ligand as the lightly n-type nature for small bandgap PbS CQDs moves towards intrinsic to even p-type behavior for large bandgap. These results align with reports claiming that p-type behavior in PbS CQD can be achieved with BDT ligands by controlled oxygen exposure [4,7]. The inert nature of gold minimizes film-substrate interactions; thus the large shift in the ionization energy (~0.5 eV) in BDT-capped PbS CQD compared to ZnI_2 MPA is attributed to the dipole interaction between CQDs and ligands as reported by previous studies [25,35,36]. Although energy levels can be shifted by charge transfer in the presence of metallic lead (Pb^0, 137.3 eV) as Zhang et al. emphasized [36], the absence of metallic shoulder in Pb4f7/2 and Pb4f5/2 peaks (Figure S3) excludes this possibility in this case.

The heavily n-doped nature of multi-step coated PbS CQD thin films with halide ligands in Figure 5 and the fact that the expected populated DOS may go undetected by photoemission due to the intrinsic low conduction band edge of CQDs indicate the possibility of potential degenerate doping ($|E_F-E_{VBM}|>E_g$, as measured) in 1-step coated thin films. Zhang et. al referred such energy band structure as degenerate/high doping based on the intraband absorption observed by Ramiro et al. in heavily n-doped SWIR PbS CQD thin films [35,36]. Less electronic coupling between the adjacent CQDs, localized wavefunctions (pronounced quantum confinement) and surface states in poorly packed CQD films can allow more discrete and larger energy spacing between intraband states

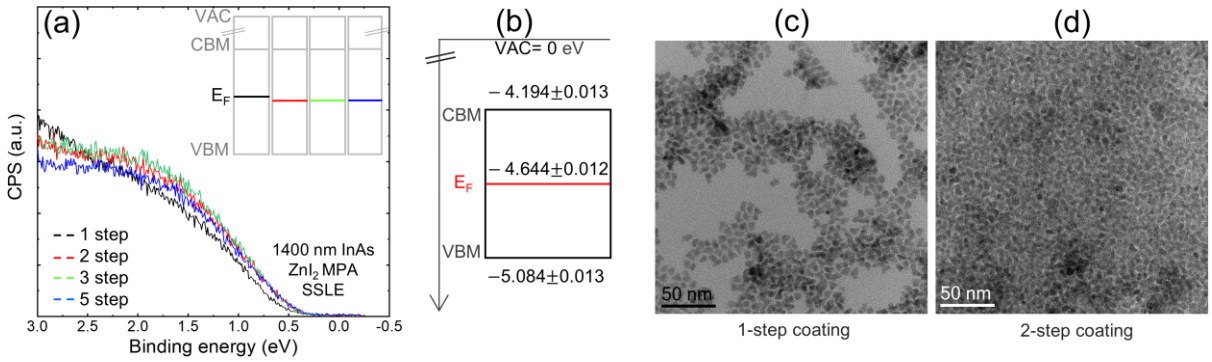


Figure 6. (a) UPS valence band edge spectra and (inset) $|E_F\text{-}E_{VBM}|$ for 1, 2, 3 and 5 step deposited SSLE InAs (1400 nm) ZnI_2 MPA thin films. (b) Full energy band structure for 2, 3 and 5 step deposited films. (c)-(d) The TEM micrographs of 1 and 2 step coated films.

[35,45–47]. Contrarily, in highly packed and thicker films (2 or more step-coated), the quantum dots are more tightly coupled, and their electronic wavefunctions overlap more significantly, forming a more continuous electronic structure [45,46,48,49]. Such delocalized mini bands rather than isolated energy levels reduce the influence of individual quantum dot surface states, which allows the doping to spread out across the entire continuous film thus diminishing the degenerate doping behavior. The absence of $|E_F\text{-}E_{VBM}|>E_g$ in BDT treated PbS and InAs (Figure 6) CQD thin films further supports this argument as the doping concentration is significantly lower than the halide ligands. Nevertheless, this work strongly suggests the energy band structure deduced from poorly packed film does not represent the energy band structure of highly packed CQD films utilized for optoelectronic device fabrication.

Because of superior chemical stability, less toxicity, and promising electronic characteristics InAs CDQs have gained increased interest [1,3,12,50,51]. Many different synthesis routes and ligands (both solid and liquid phase) are continuously emerging for various optoelectronic applications, indicating the urge to study the electronic band structure of InAs CQD films [1,3,11,12,50,51]. We adopted a similar recipe to PbS SSLE with ZnI_2 MPA for InAs with the excitonic peak at 1400 nm and compared the UPS valence band spectra of 1, 2, 3, and 5-step coated thin films in Figure 6a.

Herein, the UPS spectra shape and linear regressions are the same for the 2, 3, and 5-step coated films resulting $|E_F-E_{VBM}|$ values at ~$E_g/2$ (intrinsic behavior). Similarly, we denote that the larger $|E_F-E_{VBM}|$ (inset of Figure 6a) for 1-step coated film leading to a lightly n-doped layer is due to lack of VBM DOS resulting from poor CDQ dispersion and low density within the probing area. The extracted complete energy band structure is depicted in Figure 6b. These UPS-deduced energy band structures align with our XPS narrow band spectra of these films (Figure S6) as we calculated a jump of ~10% and ~7% of In3d5/2 and As3d peak intensities for 2-step spin-coated InAs CQD film with respect to one step deposited film. The TEM images (Figure 6c-d) of 1 and 2-step coated SSLE InAs thin films verify the results of UPS and XPS as the CQD coverage increases from 62.44% to 95.75%. The respective binary images of the TEM and HR-TEM micrographs are depicted in Figure S8. This systematic study based on PbS and InAs CQD thin films by SSLE with various ligands indicates that the valence band measurements and analysis of energy structure for CQD thin films deduced from photoemission spectra need to be carefully evaluated. More

importantly, the energy measurements need to be optimized for different ligands and quantum dots to ensure the reproducibility of the same results.

2.2 Liquid phase ligand exchange (LPLE)

As the name suggests, in liquid phase ligand exchange (LPLE), the ligands are exchanged in a liquid-liquid exchange process. Since no additional ligand exchange and solvent washing processes are required after the layer is deposited, the film with the desired application-specific thickness can be produced by one-step coating by adjusting the solution concentration [32,33]. These advantages make LPLE the ultimate choice for large-area active material mass fabrication processes for applications such as imagers and solar cells to ensure maximum uniformity [1,32,33]. We fabricated both In(As,P) and PbS SWIR CQD films by LPLE to study the UPS spectra deduced energy band structures. We exchange the native ligands of In(As,P) (1345 nm) in liquid phase by

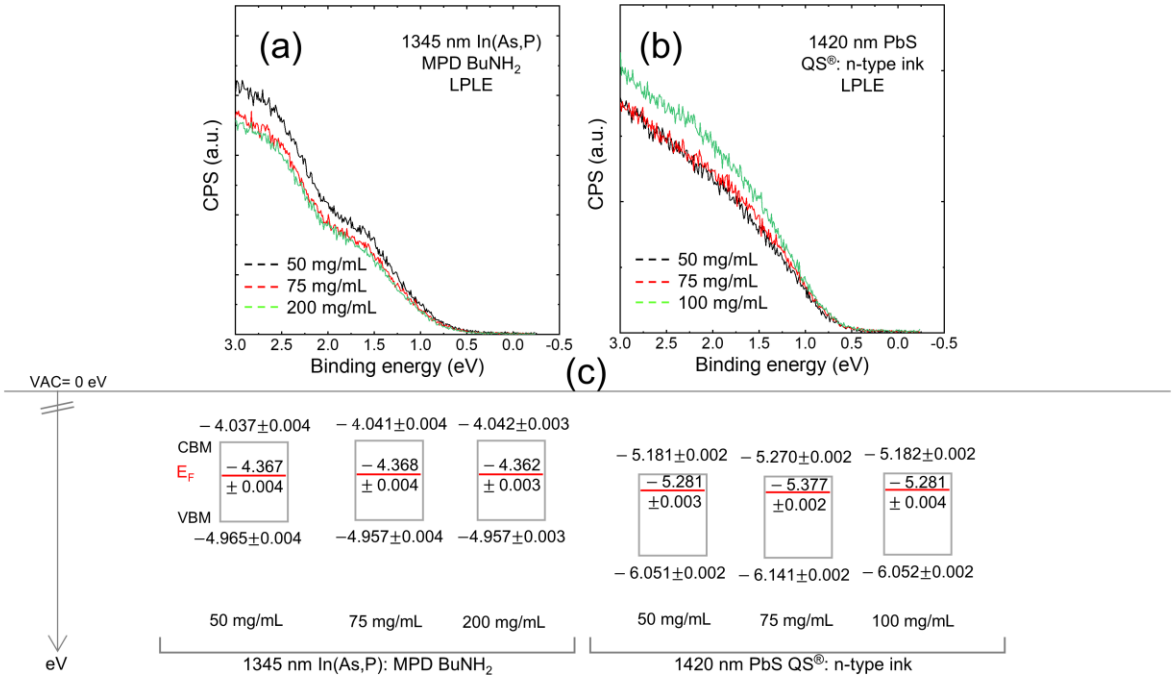


Figure 7. (a)-(b) Valence band spectra of In(As,P) and PbS CQD films prepared from various concentration (thickness) of LPLE stock solutions. Deduced energy band structures of these UPS spectra in (c). The error bars calculated from the five data points represent the precision and reproducibility.

a mixture of 3-mercapto-1,2-propanediol (MPD) and n-butylamine (n-$BuNH_2$) which we adapted from the LPLE process of In(As,P) reported by Leemans et al. [1]. On the other hand, we purchased commercially available n-type PbS (1400 nm) ink from Quantum Solutions ® that is already LPLE with I ions. The LPLE In(As,P) and PbS parent solutions are 200 mg/mL and 100 mg/mL, respectively, which are then diluted to 75 mg/mL and 50 mg/mL to assess if the thicknesses can affect the UPS measurements and derived energy band structures. It is clear from Figure 7a-b that the shape of the VBM edge and the extracted $|E_F-E_{VBM}|$ are independent of the thicknesses for both In(As,P) and PbS CQDs. In contrast to earlier UPS measurements of SSLE CQD films, where the dispersion and dot density of single-step coated films show an overestimation of $|E_F-E_{VBM}|$, we achieve reproducible spectra for CQD films produced by single-step coating by LPLE, and this for various thicknesses, indicating a better dispersion and density of CQDs films by LPLE. Acquired narrow band XPS spectra (Figure S7a-d) of LPLE PbS and In(As,P) CQD thin films fabricated from various solution concentrations reveal negligible changes in the peak signal intensities of Pb4f7/2, S2s, and In3d5/2, As3d. Energy band structures (Figure 7c) deduced from these UPS remain consistent across various concentrations of the CQD solution, revealing a lightly doped n-type In(As,P) layer and a relatively highly doped n-type PbS layer. Note that, the result of In(As,P) energy band structure is well in line with the report by Leemans et. al [1]. At the same time, our multi-step deposited SSLE PbS ZnI_2 MPA energy band structure is in line with the commercially purchased n-type PbS ink with LPLE with the iodine ion-containing ligand.

2.3 Demonstration of thin-film SWIR SSLE PbS and LPLE In(As,P) CDQ photodiodes

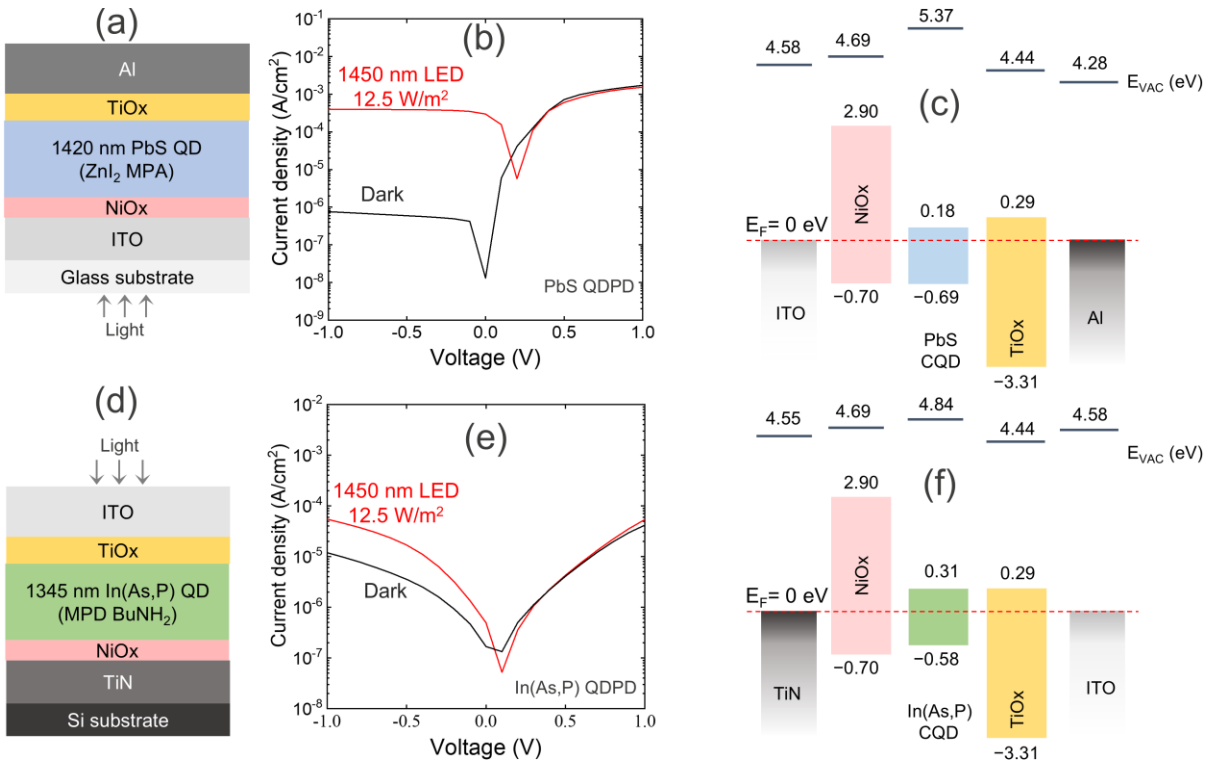


Figure 8. Thin-film SWIR photodiode architecture, (b)-(c) current-voltage characteristics under dark condition and (e)-(f) Fermi-referenced energy band diagrams of PbS QDPD (a-c) and, In(As,P) QDPD (d-f), respectively.

Energy band structures of thin-film materials lie at the heart of thin-film optoelectronic device architecture. It is crucial to model the energy band diagram of the full thin film stack including band alignments, barriers, and bending in order to improve our understanding of devices [25,28,52]. Also, it is equally important to study the origin, distribution, and density of bulk and interface trap states as they can be severely detrimental to the device characteristics even if good band alignments are achieved [52].

We fabricate QDPD photodiodes featuring p-type NiOx and n-type CQD layers of PbS (Figure 8a) and In(As,P) (Figure 8d), respectively. The dark and light (AM1.5G) current-voltage (J-V) characteristics (Figure 8b,e) of both PbS and In(As,P) QDPD demonstrate PN junction behavior ($J_{Forward} > J_{Reserve}$) which validates our UPS spectra deduced $|E_F\text{-}E_{VBM}|$ estimations. Since all

heterostructures undergo Fermi level alignments to achieve thermodynamic equilibrium, it is very important to include the Fermi energy level (work function, WF) to achieve a complete energy band diagram of full thin film stack [53,54]. However, very often vacuum-referenced energy band diagram (Figure S9) with only ionization energy (IE) and electron affinity (EA) are measured [6,14]. In contrast, our proposed UPS measurement method allows us to extract complete energy band structures (IE, WF, and EA) of thin film CQDs. The complete energy band structures of full PbS (Figure 8c) and In(As,P) (Figure 8f) QDPD stacks including electron and hole transport layers and contacts are measured and plotted with respect to the Fermi energy. Energy band structures of Al, TiOx, and ITO are referenced from our previous reports[1,52], while the NiOx is characterized by UPS as shown in Figure S11. Both stacks show a favorable energy band alignment for the extraction of dark and photo-generated electrons and holes. These energy band models can be further leveraged to fine-tune the band alignments across the full stacks including the selection of an energetically favorable hole transport layer and interfacial layers for efficient electronic transport. It is also crucial to pair detailed trap characteristics within the thin film QDPD stack with the energy band structure model to obtain a model of both dark and photo carrier transport [52]. Accurate energy levels of isolated layers are an essential first step toward constructing comprehensive energy band models of complete photodiode stacks. We believe further efforts are needed to achieve an accurate energy band diagram that accounts for interface effects including dipole moments, charge transfer, and electrostatics between layers, by measuring the energy structure at each step of the photodiode stack fabrication.

3. CONCLUSION

We present accurate band structure measurements of SWIR PbS and InAs CQD thin films treated with various ligands by solid and liquid phase ligand exchanges. Despite having the average

thickness of CQD thin films well over photoemission information depth, it is the CQD packing density and respective wavefunction overlap between neighboring dots within the probing area that need to be optimized to achieve a precise $|E_F-E_{VBM}|$ determination of bulk CQD films. High-resolution TEM images confirm a CQD coverage area of 90.62 % for optimized multi-step coated film compared to 53.28 % for single-step deposited film which resulted in a consistent $|E_F-E_{VBM}|$ estimation for PbS and InAs with various sizes and ligands by solid-state ligand exchange process. The XPS narrow band spectra, AFM, and ellipsometry results are in line with TEM and UPS measurements. The XPS narrow band spectra analysis confirms that the liquid phase ligand exchange yields compact thin films fabricated from solutions of varying concentrations. This is also reflected in the UPS extracted $|E_F-E_{VBM}|$ values. We also fabricate and demonstrate SWIR thin-film photodiodes based on PbS and In(As,P) active layers to validate our measured energy band structure models. Overall, this study provides solid evidence and methodology to advance the knowledge of how to properly measure and deduce the energy band structures of PbS and InAs CQD for thin-film SWIR sensing applications. A bridge between the electronic band structure, device geometrics, and performance also paves the way for efficient optimization of thin-film SWIR detectors.

4. EXPERIMENT

All PbS CQDs (absorbing at 1520, 1420, 1280, and 940 nm) and InAs (1400) are purchased from Quantum Solutions ® in octane. The stock solution was then first diluted to 40 mg/mL as it optimized for SSLE for our thin film photodetector applications [7,13,22]. The halide ligand solutions as Zn-X_2 (I_2, Br_2, and Cl_2) were prepared by mixing with 0.01% MPA in ethanol and the stock solution of BDT in acetonitrile. All the CDQ films were spin-coated on the Au-coated Si substrate at 2500 rpm for 15 s. The solution of Zn-halide MPA was dispersed by pipet on the PbS film and

left for 5 sec to exchange the ligands. The substrate was then spun dry and subsequently flushed with ethanol twice. For SSLE of 2, 3, and 5-step coating, the process was repeated at 30 s interval time to let the substrate dry. The same process was adapted to fabricate PbS BDT films except the ligand exchange time was 30 s instead of 5 s for halide ions. The SSLE of InAs with ZnI_2 MPA was prepared using the same ligand stock solution and process flow as PbS.

The LPLE n-type PbS (1400 nm) ink solution was purchased from Quantum Solutions ® as 100 mg/mL. The parent stock solution of 100 mg/mL and diluted 75 mg/mL and 50 mg/mL are directly deposited by spin coating at 1000 rpm for 15 s. For detailed synthesis and liquid-liquid ligand exchange process flow of In(As,P) MPD $BuNH_2$ we refer to the report by Leemans et al. [1]. Dilutions of stock solution (200 mg/mL) to 75 mg/mL and 50 mg/mL were made to study the thickness effect of UPS spectra and deduced energy band structures. All the films (both SSLE and LPLE) were annealed at 80°C for 10 minutes on the hotplate inside the glove box.

The X-ray and ultraviolet spectroscopy (XPS and UPS) measurements were carried out using the VersaProbe III instrument from Physical Electronics. The tool is equipped with monochromatized Al K-alpha (1486.6 eV) and He I (21.2 eV) UV radiation for XPS and UPS sources, respectively. The XPS spectra were acquired by 100×100 μm^2 X-ray beam spot size with the flood gun turned on while the UPS spectra were recorded by a 1 mm^2 UV beam without the flood gun. During UPS measurements a sample bias of −5 V was applied during all the measurements to detect the secondary electron (SE) emission edge. The energy resolution of the UPS spectrometer is ~100 meV, measured as the width of the Fermi edge from Ag and Au calibration at room temperature Figure S10a-b. All post-processing of XPS and UPS spectra was performed using MultiPak (data reduction software for XPS and AES by ULVAC-PHI). The error bars for absolute energy values in Figures 5, 6, and 7 are calculated from five data points, representing measurement precision and

reproducibility, as shown in Figure S12. To preserve accuracy of energy band structure measurements, substrate with non-reactive, and stable surface properties is essential to avoid any potential substrate-sample interactions. Herein, the substrates for XPS/UPS measurements were carefully prepared by depositing Au on a heavily doped Si substrate and then diced to the desired size. The substrates, with the sample films on top, were mounted using Au-coated stainless-steel washers from all four corners to ensure good electrical contact as demonstrated in the inset of Figure S10a.

The transmission electron microscopy (TEM) images were taken by scanning transmission electron microscope (STEM) FEI Titan3™ G2 60-300 S/TEM at 200 KV. The image processing of TEM images was performed using MATLAB binary imaging tool. The ellipsometry measurements were done using an RC2 Ellipsometer by J.A. Woolam. The AFM topographies were acquired using a dimension edge scanning probe microscope manufactured by Bruker.

The thin film PbS and In(As,P) QDPDs were developed on a glass substrate with pre-pattern ITO stripes and a Silicon substrate with pre-pattern TiN as transparent bottom electrodes, respectively. The substrates were sequentially cleaned using acetone, and isopropanol in an ultrasonic bath at 50°C. A thin (15 nm) NiOx film was then sputter deposited as the hole transport layer (HTL) layer from a metallic nickel target using oxygen plasma by a Nebula system (Angstrom Engineering Inc.). Subsequently, the film was annealed at 300°C for 10 minutes on the hotplate under ambient conditions. For PbS QDPD, the SSLE process of ZnI_2 MPA was utilized as described earlier and repeated 14 times to achieve a total active layer thickness of >350 nm. The LPLE In(As,P) MPD $BuNH_2$ was deposited as the active layer of In(As,P) QDPD by spin coating from 200 mg/mL stock solution which makes ~180 nm thick active layer. Both active layers were annealed at 80°C for 10 minutes. A 20 nm thick electron beam evaporated TiOx was coated using a shadow mask

on the active layers as the electron transport layer (ETL). Finally, the PbS and In(As,P) QDPDs were completed with 200 nm thick Al and 100 nm thick ITO as top electrodes, respectively, using a shadow mask by thermal evaporation.

ASSOCIATED CONTENT

Supporting Information

Variable angle spectroscopic ellipsometry, UPS spectra, XPS narrow band spectra, EDS elemental map, AFM images, TEM micrographs, device schematics, energy band diagrams, UPS sample setup, optical bandgaps and $|E_F-E_{VBM}|$

AUTHOR INFORMATION

Corresponding Authors

Abu Bakar Siddik- IMEC, Kapeldreef 75, 3001 Leuven, Belgium, and Department of Electrical Engineering ESAT, KU Leuven, Kasteelpark Arenberg 10, 3001 Leuven, Belgium.

abu.bakar.siddik@imec.be

Epimitheas Georgitzikis- IMEC, Kapeldreef 75, 3001 Leuven, Belgium.

epimitheas.georgitzikis@imec.be

Author Contributions

The manuscript was written through the contributions of all authors. All authors have given approval to the final version of the manuscript.

Notes

The authors declare no competing financial interest.

ACKNOWLEDGMENT

We would like to acknowledge the support from the QustomDot for providing the liquid phase ligand exchanged In(As,P) quantum dots utilized in this study.

REFERENCES

(1) Leemans, J.; Pejović, V.; Georgitzikis, E.; Minjauw, M.; Siddik, A. B.; Deng, Y.; Kuang, Y.; Roelkens, G.; Detavernier, C.; Lieberman, I.; Malinowski, P. E.; Cheyns, D.; Hens, Z. Colloidal III–V Quantum Dot Photodiodes for Short-Wave Infrared Photodetection. *Advanced Science* **2022**, *9* (17), 2200844. https://doi.org/10.1002/advs.202200844.

(2) Wu, Z.; Ou, Y.; Cai, M.; Wang, Y.; Tang, R.; Xia, Y. Short-Wave Infrared Photodetectors and Imaging Sensors Based on Lead Chalcogenide Colloidal Quantum Dots. *Advanced Optical Materials* **2023**, *11* (1), 2201577. https://doi.org/10.1002/adom.202201577.

(3) Zhao, X.; Lim, L. J.; Ang, S. S.; Tan, Z. Efficient Short-Wave Infrared Light-Emitting Diodes Based on Heavy-Metal-Free Quantum Dots. *Advanced Materials* **2022**, *34* (45), 2206409. https://doi.org/10.1002/adma.202206409.

(4) Bi, Y.; Pradhan, S.; Gupta, S.; Akgul, M. Z.; Stavrinadis, A.; Konstantatos, G. Infrared Solution-Processed Quantum Dot Solar Cells Reaching External Quantum Efficiency of 80% at 1.35 Mm and J_{sc} in Excess of 34 mA Cm $^{-2}$. *Advanced Materials* **2018**, *30* (7), 1704928. https://doi.org/10.1002/adma.201704928.

(5) Bederak, D.; Balazs, D. M.; Sukharevska, N. V.; Shulga, A. G.; Abdu-Aguye, M.; Dirin, D. N.; Kovalenko, M. V.; Loi, M. A. Comparing Halide Ligands in PbS Colloidal Quantum Dots for Field-Effect Transistors and Solar Cells. *ACS Appl. Nano Mater.* **2018**, *1* (12), 6882–6889. https://doi.org/10.1021/acsanm.8b01696.

(6) Vafaie, M.; Fan, J. Z.; Morteza Najarian, A.; Ouellette, O.; Sagar, L. K.; Bertens, K.; Sun, B.; García de Arquer, F. P.; Sargent, E. H. Colloidal Quantum Dot Photodetectors with 10-Ns Response Time and 80% Quantum Efficiency at 1,550 Nm. *Matter* **2021**, *4* (3), 1042–1053. https://doi.org/10.1016/j.matt.2020.12.017.

(7) Pejović, V.; Georgitzikis, E.; Lieberman, I.; Malinowski, P. E.; Heremans, P.; Cheyns, D. Photodetectors Based on Lead Sulfide Quantum Dot and Organic Absorbers for Multispectral Sensing in the Visible to Short-Wave Infrared Range. *Adv Funct Materials* **2022**, *32* (28), 2201424. https://doi.org/10.1002/adfm.202201424.

(8) Choi, H. T.; Kang, J.-H.; Ahn, J.; Jin, J.; Kim, J.; Park, S.; Kim, Y.-H.; Kim, H.; Song, J. D.; Hwang, G. W.; Im, S.; Shim, W.; Lee, Y. T.; Park, M.-C.; Hwang, D. K. Zero-Dimensional PbS Quantum Dot–InGaZnO Film Heterostructure for Short-Wave Infrared Flat-Panel Imager. *ACS Photonics* **2020**, *7* (8), 1932–1941. https://doi.org/10.1021/acsphotonics.0c00594.

(9) Malinowski, P. E.; Pejović, V.; Lieberman, I.; Kim, J. H.; Siddik, A. B.; Georgitzikis, E.; Lim, M. J.; Moreno Hagelsieb, L.; Hermans, Y.; Pintor Monroy, I.; Song, W.; Basak, S.; Gehlhaar, R.; De Roose, F.; Siskos, A.; Papadopoulos, N.; Thijs, S.; Vershooten, T.; Chandrasekaran, N.; Li, Y.; Soussan, P.; Genoe, J.; Heremans, P.; Lee, J.; Cheyns, D. Image

Sensors Using Thin-Film Absorbers. *Appl. Opt.* **2023**, *62* (17), F21. https://doi.org/10.1364/AO.485552.
(10) McDonald, S. A.; Konstantatos, G.; Zhang, S.; Cyr, P. W.; Klem, E. J. D.; Levina, L.; Sargent, E. H. Solution-Processed PbS Quantum Dot Infrared Photodetectors and Photovoltaics. *Nature Mater* **2005**, *4* (2), 138–142. https://doi.org/10.1038/nmat1299.
(11) Xia, P.; Sun, B.; Biondi, M.; Xu, J.; Atan, O.; Imran, M.; Hassan, Y.; Liu, Y.; Pina, J. M.; Najarian, A. M.; Grater, L.; Bertens, K.; Sagar, L. K.; Anwar, H.; Choi, M.; Zhang, Y.; Hasham, M.; García de Arquer, F. P.; Hoogland, S.; Wilson, M. W. B.; Sargent, E. H. Sequential Co-Passivation in InAs Colloidal Quantum Dot Solids Enables Efficient Near-Infrared Photodetectors. *Advanced Materials* **2023**, *35* (28), 2301842. https://doi.org/10.1002/adma.202301842.
(12) Vafaie, M.; Morteza Najarian, A.; Xu, J.; Richter, L. J.; Li, R.; Zhang, Y.; Imran, M.; Xia, P.; Ban, H. W.; Levina, L.; Singh, A.; Meitzner, J.; Pattantyus-Abraham, A. G.; García de Arquer, F. P.; Sargent, E. H. Molecular Surface Programming of Rectifying Junctions between InAs Colloidal Quantum Dot Solids. *Proc. Natl. Acad. Sci. U.S.A.* **2023**, *120* (41), e2305327120. https://doi.org/10.1073/pnas.2305327120.
(13) Pejovic, V.; Lee, J.; Georgitzikis, E.; Li, Y.; Kim, J. H.; Lieberman, I.; Malinowski, P. E.; Heremans, P.; Cheyns, D. Thin-Film Photodetector Optimization for High-Performance Short-Wavelength Infrared Imaging. *IEEE Electron Device Lett.* **2021**, *42* (8), 1196–1199. https://doi.org/10.1109/LED.2021.3093081.
(14) Georgitzikis, E.; Malinowski, P. E.; Maes, J.; Hadipour, A.; Hens, Z.; Heremans, P.; Cheyns, D. Optimization of Charge Carrier Extraction in Colloidal Quantum Dots Short-Wave Infrared Photodiodes through Optical Engineering. *Adv Funct Materials* **2018**, *28* (42), 1804502. https://doi.org/10.1002/adfm.201804502.
(15) Peng, L.; Wang, Y.; Ren, Y.; Wang, Z.; Cao, P.; Konstantatos, G. InSb/InP Core–Shell Colloidal Quantum Dots for Sensitive and Fast Short-Wave Infrared Photodetectors. *ACS Nano* **2024**, *18* (6), 5113–5121. https://doi.org/10.1021/acsnano.3c12007.
(16) Seo, H.; Eun, H. J.; Lee, A. Y.; Lee, H. K.; Kim, J. H.; Kim, S. Colloidal InSb Quantum Dots for 1500 Nm SWIR Photodetector with Antioxidation of Surface. *Advanced Science* **2024**, *11* (4), 2306439. https://doi.org/10.1002/advs.202306439.
(17) Liu, Y.; Li, F.; Shi, G.; Liu, Z.; Lin, X.; Shi, Y.; Chen, Y.; Meng, X.; Lv, Y.; Deng, W.; Pan, X.; Ma, W. PbSe Quantum Dot Solar Cells Based on Directly Synthesized Semiconductive Inks. *ACS Energy Lett.* **2020**, *5* (12), 3797–3803. https://doi.org/10.1021/acsenergylett.0c02011.
(18) Yang, J.; Hu, H.; Lv, Y.; Yuan, M.; Wang, B.; He, Z.; Chen, S.; Wang, Y.; Hu, Z.; Yu, M.; Zhang, X.; He, J.; Zhang, J.; Liu, H.; Hsu, H.-Y.; Tang, J.; Song, H.; Lan, X. Ligand-Engineered HgTe Colloidal Quantum Dot Solids for Infrared Photodetectors. *Nano Lett.* **2022**, *22* (8), 3465–3472. https://doi.org/10.1021/acs.nanolett.2c00950.
(19) Sloboda, T.; Svanström, S.; Johansson, F. O. L.; Bryngelsson, E.; García-Fernández, A.; Lindblad, A.; Cappel, U. B. The Impact of Chemical Composition of Halide Surface Ligands on the Electronic Structure and Stability of Lead Sulfide Quantum Dot Materials. *Phys. Chem. Chem. Phys.* **2022**, *24* (20), 12645–12657. https://doi.org/10.1039/D2CP01050J.
(20) Chuang, C.-H. M.; Brown, P. R.; Bulović, V.; Bawendi, M. G. Improved Performance and Stability in Quantum Dot Solar Cells through Band Alignment Engineering. *Nature Mater* **2014**, *13* (8), 796–801. https://doi.org/10.1038/nmat3984.

(21) Yang, M.; Liu, H.; Wen, S.; Du, Y.; Gao, F. Optimizing the Infrared Photoelectric Detection Performance of Pbs Quantum Dots through Solid-State Ligand Exchange. *Materials* **2022**, *15* (24), 9058. https://doi.org/10.3390/ma15249058.
(22) Lee, J.; Georgitzikis, E.; Hermans, Y.; Papadopoulos, N.; Chandrasekaran, N.; Jin, M.; Siddik, A. B.; De Roose, F.; Uytterhoeven, G.; Kim, J. H.; Puybaret, R.; Li, Y.; Pejovic, V.; Karve, G.; Cheyns, D.; Genoe, J.; Malinowski, P. E.; Heremans, P.; Myny, K. Thin-Film Image Sensors with a Pinned Photodiode Structure. *Nat Electron* **2023**, *6* (8), 590–598. https://doi.org/10.1038/s41928-023-01016-9.
(23) Wang, R.; Shang, Y.; Kanjanaboos, P.; Zhou, W.; Ning, Z.; Sargent, E. H. Colloidal Quantum Dot Ligand Engineering for High Performance Solar Cells. *Energy Environ. Sci.* **2016**, *9* (4), 1130–1143. https://doi.org/10.1039/C5EE03887A.
(24) Fan, J. Z.; Andersen, N. T.; Biondi, M.; Todorović, P.; Sun, B.; Ouellette, O.; Abed, J.; Sagar, L. K.; Choi, M.; Hoogland, S.; de Arquer, F. P. G.; Sargent, E. H. Mixed Lead Halide Passivation of Quantum Dots. *Advanced Materials* **2019**, *31* (48), 1904304. https://doi.org/10.1002/adma.201904304.
(25) Brown, P. R.; Kim, D.; Lunt, R. R.; Zhao, N.; Bawendi, M. G.; Grossman, J. C.; Bulović, V. Energy Level Modification in Lead Sulfide Quantum Dot Thin Films through Ligand Exchange. *ACS Nano* **2014**, *8* (6), 5863–5872. https://doi.org/10.1021/nn500897c.
(26) Li, M.; Zhao, X.; Zhang, A.; Wang, B.; Yang, Y.; Xu, S.; Hu, Q.; Liang, G.; Xiao, Z.; Gao, L.; Zhang, J.; Hsu, H.-Y.; Song, H.; Tang, J. Organic Ligand Complementary Passivation to Colloidal-Quantum-Dot Surface Enables Efficient Infrared Solar Cells. *Chemical Engineering Journal* **2023**, *455*, 140961. https://doi.org/10.1016/j.cej.2022.140961.
(27) Miller, E. M.; Kroupa, D. M.; Zhang, J.; Schulz, P.; Marshall, A. R.; Kahn, A.; Lany, S.; Luther, J. M.; Beard, M. C.; Perkins, C. L.; van de Lagemaat, J. Revisiting the Valence and Conduction Band Size Dependence of PbS Quantum Dot Thin Films. *ACS Nano* **2016**, *10* (3), 3302–3311. https://doi.org/10.1021/acsnano.5b06833.
(28) Song, J. H.; Choi, H.; Pham, H. T.; Jeong, S. Energy Level Tuned Indium Arsenide Colloidal Quantum Dot Films for Efficient Photovoltaics. *Nat Commun* **2018**, *9* (1), 4267. https://doi.org/10.1038/s41467-018-06399-4.
(29) Kirmani, A. R.; Walters, G.; Kim, T.; Sargent, E. H.; Amassian, A. Optimizing Solid-State Ligand Exchange for Colloidal Quantum Dot Optoelectronics: How Much Is Enough? *ACS Appl. Energy Mater.* **2020**, *3* (6), 5385–5392. https://doi.org/10.1021/acsaem.0c00389.
(30) Carey, G. H.; Chou, K. W.; Yan, B.; Kirmani, A. R.; Amassian, A.; Sargent, E. H. Materials Processing Strategies for Colloidal Quantum Dot Solar Cells: Advances, Present-Day Limitations, and Pathways to Improvement. *MRS Communications* **2013**, *3* (2), 83–90. https://doi.org/10.1557/mrc.2013.17.
(31) You, H. R.; Park, J. Y.; Lee, D. H.; Kim, Y.; Choi, J. Recent Research Progress in Surface Ligand Exchange of PbS Quantum Dots for Solar Cell Application. *Applied Sciences* **2020**, *10* (3), 975. https://doi.org/10.3390/app10030975.
(32) Balazs, D. M.; Rizkia, N.; Fang, H.-H.; Dirin, D. N.; Momand, J.; Kooi, B. J.; Kovalenko, M. V.; Loi, M. A. Colloidal Quantum Dot Inks for Single-Step-Fabricated Field-Effect Transistors: The Importance of Postdeposition Ligand Removal. *ACS Appl. Mater. Interfaces* **2018**, *10* (6), 5626–5632. https://doi.org/10.1021/acsami.7b16882.
(33) Wang, L.; Wang, Y.; Jia, Y.; Liu, X.; Liu, T.; Fu, T.; Li, J.; Weng, B.; Zhang, X.; Liu, Y. Manipulation of Phase-Transfer Ligand-Exchange Dynamics of PbS Quantum Dots for

Efficient Infrared Photovoltaics. *J. Phys. Chem. C* **2019**, *123* (50), 30137–30144. https://doi.org/10.1021/acs.jpcc.9b09231.
(34) Whitten, J. E. Ultraviolet Photoelectron Spectroscopy: Practical Aspects and Best Practices. *Applied Surface Science Advances* **2023**, *13*, 100384. https://doi.org/10.1016/j.apsadv.2023.100384.
(35) Ramiro, I.; Kundu, B.; Dalmases, M.; Özdemir, O.; Pedrosa, M.; Konstantatos, G. Size- and Temperature-Dependent Intraband Optical Properties of Heavily n-Doped PbS Colloidal Quantum Dot Solid-State Films. *ACS Nano* **2020**, *14* (6), 7161–7169. https://doi.org/10.1021/acsnano.0c02033.
(36) Zhang, H.; Ledos, N.; Cavallo, M.; Bossavit, E.; Khalili, A.; Curti, L.; Xu, X. Z.; Dandeu, E.; Utterback, J. K.; Ithurria, S.; Delerue, C.; Pierucci, D.; Dudin, P.; Avila, J.; Silly, M. G.; Lhuillier, E. Photoemission Insight on Narrow Band Gap PbS Quantum Dots Relevant for Infrared Imaging. *J. Phys. Chem. C* **2024**, *128* (5), 2028–2036. https://doi.org/10.1021/acs.jpcc.3c07499.
(37) Sloboda, T.; Johansson, F. O. L.; Kammlander, B.; Berggren, E.; Svanström, S.; Fernández, A. G.; Lindblad, A.; Cappel, U. B. Unravelling the Ultrafast Charge Dynamics in PbS Quantum Dots through Resonant Auger Mapping of the Sulfur K-Edge. *RSC Adv.* **2022**, *12* (49), 31671–31679. https://doi.org/10.1039/D2RA06091D.
(38) Choi, G.-S.; Lim, M. J.; Sutcu, I.; Yu, J.; Malinowski, P.; Lee, S. Y.; Lieberman, I. Tailoring of Colloidal Quantum Dot Layer Thickness for Highly Efficient Short-Wavelength Infrared Photodiode. *Applied Physics Letters* **2024**, *124* (12), 121103. https://doi.org/10.1063/5.0188574.
(39) Hodroj, A.; Roussel, H.; Crisci, A.; Robaut, F.; Gottlieb, U.; Deschanvres, J. L. Density, Thickness and Composition Measurements of TiO2SiO2 Thin Films by Coupling X-Ray Reflectometry, Ellipsometry and Electron Probe Microanalysis-X. *Applied Surface Science* **2006**, *253* (1), 363–366. https://doi.org/10.1016/j.apsusc.2006.06.014.
(40) She, C.; Fedin, I.; Dolzhnikov, D. S.; Demortière, A.; Schaller, R. D.; Pelton, M.; Talapin, D. V. Low-Threshold Stimulated Emission Using Colloidal Quantum Wells. *Nano Lett.* **2014**, *14* (5), 2772–2777. https://doi.org/10.1021/nl500775p.
(41) Dibenedetto, C. N.; Fanizza, E.; Brescia, R.; Kolodny, Y.; Remennik, S.; Panniello, A.; Depalo, N.; Yochelis, S.; Comparelli, R.; Agostiano, A.; Curri, M. L.; Paltiel, Y.; Striccoli, M. Coupling Effects in QD Dimers at Sub-Nanometer Interparticle Distance. *Nano Res.* **2020**, *13* (4), 1071–1080. https://doi.org/10.1007/s12274-020-2747-3.
(42) Li, H.; Ding, C.; Oguri, N.; Makino, Y.; Liu, D.; Guo, Y.; Wei, Y.; Li, Y.; Yang, Y.; Wang, D.; Chen, S.; Masuda, T.; Hayase, S.; Sogabe, T.; Shen, Q. Elucidating the Mechanisms of the Large Stokes Shift in Isolated and Coupled PbS Quantum Dots. *J. Phys. Chem. C* **2024**, *128* (21), 8732–8740. https://doi.org/10.1021/acs.jpcc.4c02008.
(43) Bederak, D.; Balazs, D. M.; Sukharevska, N. V.; Shulga, A. G.; Abdu-Aguye, M.; Dirin, D. N.; Kovalenko, M. V.; Loi, M. A. Comparing Halide Ligands in PbS Colloidal Quantum Dots for Field-Effect Transistors and Solar Cells. *ACS Appl. Nano Mater.* **2018**, *1* (12), 6882–6889. https://doi.org/10.1021/acsanm.8b01696.
(44) Crisp, R. W.; Kroupa, D. M.; Marshall, A. R.; Miller, E. M.; Zhang, J.; Beard, M. C.; Luther, J. M. Metal Halide Solid-State Surface Treatment for High Efficiency PbS and PbSe QD Solar Cells. *Sci Rep* **2015**, *5* (1), 9945. https://doi.org/10.1038/srep09945.
(45) Cademartiri, L.; Ozin, G. A.; Lehn, J.-M. *Concepts of Nanochemistry*; Wiley-VCH Verlag GmbH & Co. KGaA: Weinheim, 2009.

(46) *Nanocrystal Quantum Dots*, 2nd ed.; Klimov, V. I., Ed.; CRC Press, 2017. https://doi.org/10.1201/9781420079272.
(47) Houtepen, A. J.; Hens, Z.; Owen, J. S.; Infante, I. On the Origin of Surface Traps in Colloidal II–VI Semiconductor Nanocrystals. *Chem. Mater.* **2017**, *29* (2), 752–761. https://doi.org/10.1021/acs.chemmater.6b04648.
(48) Kagan, C. R.; Murray, C. B. Charge Transport in Strongly Coupled Quantum Dot Solids. *Nature Nanotech* **2015**, *10* (12), 1013–1026. https://doi.org/10.1038/nnano.2015.247.
(49) Liu, Y.; Peard, N.; Grossman, J. C. Bandlike Transport in PbS Quantum Dot Superlattices with Quantum Confinement. *J. Phys. Chem. Lett.* **2019**, *10* (13), 3756–3762. https://doi.org/10.1021/acs.jpclett.9b01282.
(50) Kim, S.; Yeon, S.; Lee, M.; Jin, J.; Shin, S.; Gwak, N.; Jeong, I.; Jang, H.; Hwang, G. W.; Oh, N. Chemically and Electronically Active Metal Ions on InAs Quantum Dots for Infrared Detectors. *NPG Asia Mater* **2023**, *15* (1), 30. https://doi.org/10.1038/s41427-023-00477-w.
(51) Sun, B.; Najarian, A. M.; Sagar, L. K.; Biondi, M.; Choi, M.; Li, X.; Levina, L.; Baek, S.; Zheng, C.; Lee, S.; Kirmani, A. R.; Sabatini, R.; Abed, J.; Liu, M.; Vafaie, M.; Li, P.; Richter, L. J.; Voznyy, O.; Chekini, M.; Lu, Z.; García de Arquer, F. P.; Sargent, E. H. Fast Near-Infrared Photodetection Using III–V Colloidal Quantum Dots. *Advanced Materials* **2022**, *34* (33), 2203039. https://doi.org/10.1002/adma.202203039.
(52) Siddik, A. B.; Georgitzikis, E.; Hermans, Y.; Kang, J.; Kim, J. H.; Pejovic, V.; Lieberman, I.; Malinowski, P. E.; Kadashchuk, A.; Genoe, J.; Conard, T.; Cheyns, D.; Heremans, P. Interface-Engineered Organic Near-Infrared Photodetector for Imaging Applications. *ACS Appl. Mater. Interfaces* **2023**, *15* (25), 30534–30542. https://doi.org/10.1021/acsami.3c03708.
(53) Volk, S.; Yazdani, N.; Yarema, O.; Yarema, M.; Bozyigit, D.; Wood, V. *In Situ* Measurement and Control of the Fermi Level in Colloidal Nanocrystal Thin Films during Their Fabrication. *J. Phys. Chem. Lett.* **2018**, *9* (24), 7165–7172. https://doi.org/10.1021/acs.jpclett.8b03283.
(54) Peljo, P.; Manzanares, J. A.; Girault, H. H. Contact Potentials, Fermi Level Equilibration, and Surface Charging. *Langmuir* **2016**, *32* (23), 5765–5775. https://doi.org/10.1021/acs.langmuir.6b01282.

